*J. Fluid Mech.* (1972), *vol.* 55, *part* 4, *pp.* 677–709
*Printed in Great Britain*



# Axisymmetric slow viscous flow past an arbitrary convex body of revolution

By MICHAEL J. GLUCKMAN, SHELDON WEINBAUM AND ROBERT PFEFFER
The City College of The City University of New York

(Received 6 April 1972)

Considerable advances have been made in the past few years in treating a variety of problems in slender-body Stokes flow (Taylor 1969; Batchelor 1970; Cox 1970, 1971; Tillett 1970). However, the problem of treating the creeping motion past bluff objects, whose boundaries do not conform to a constant co-ordinate surface of one of the special orthogonal co-ordinate systems for which the Stokes slow-flow equation is simply separable, is still largely unsolved. In the slender-body Stokes flow studies mentioned above, the viscous-flow boundary-value problem is formulated approximately as an integral equation for an unknown distribution of Stokeslets over a line enclosed by the body. The theory is valid for only very extended shapes, since the error in drag decays inversely as the logarithm of the aspect ratio of the object. By contrast, the present authors show that the boundary-value problem for the axisymmetric flow past an arbitrary convex body of revolution can be formulated exactly as an integral equation for an unknown distribution of ring-like singularities over the surface of the body. The kernel in this integral equation is closely related to the fundamental separable solutions of the Stokes slow-flow equation when written in an oblate spheroidal co-ordinate system of vanishing aspect ratio. The two lowest-order appropriate spheroidal singularities are found to provide a complete description for all surface elements, except those perpendicular to the axis. Higher-order singularities of all orders are required to describe axially perpendicular surfaces, such as the ends of a cylinder or the blunt base of an object. The newly derived integral equation is solved numerically to provide the first theoretical solutions for low aspect ratio cylinders and cones. The theoretically predicted drag results are in excellent agreement with experimentally measured values.

## 1. Introduction

In the 120 years that have elapsed since Stokes's classic paper (1851) on the motion of a spherical pendulum bob in a very viscous liquid, an extensive body of literature has evolved for flows whose Reynolds number is sufficiently small for inertial forces to be neglected. A significant portion of this literature has been devoted to the creeping motion in an unbounded medium of a single object, or two spherical objects, where the boundaries conform to a co-ordinate surface of

one of the special orthogonal co-ordinate systems for which the Stokes slow-flow equation is simply separable. In the past few years these studies have been extended to include some simple multiparticle flow configurations. For example, the present authors have used a multipole truncation technique to describe the steady, axisymmetric Stokes flow past finite line arrays of spheres and spheroids with arbitrary spacing in an unbounded fluid (Gluckman, Pfeffer & Weinbaum 1971). This same technique has also been applied to the simple, unsteady three-body fluid-particle interaction problem of three spheres falling along their line of centres in a gravitational field (Gluckman, Pfeffer & Weinbaum 1972). Related truncation procedures had previously been used by Skalak and his colleagues for examining a variety of bounded axisymmetric motions with periodic boundary conditions, which were idealized models of capillary blood flow. These included the movement of an infinite line array of equally spaced spheres (Wang & Skalak 1969) and spheroids (Chen & Skalak 1970) along the axis of a circular tube with and without through-flow. In view of these advances it is perhaps quite surprising that very little progress has been made in the intervening years in describing the creeping motion past even a single object whose boundary departs significantly from one of the special natural co-ordinate surfaces. The only important exceptions are the varied problems in the slender-body Stokes flow examined by Burgers (1938), Tuck (1964), Taylor (1969), Batchelor (1970), Cox (1970, 1971), Tillet (1970) and others.

The underlying difficulty in treating the near field of the Stokes flows with complicated boundary shapes is the slow decay of disturbances produced by any boundaries in the flow field. In two dimensions this decay is logarithmic, while in three dimensions it is algebraic; in either case there is no mechanism for preventing the spread of the disturbance in all directions, unless inertial effects are included. The following two numerical examples are a graphic illustration of the far-reaching influence of boundaries on both the same and distant objects. Consider first the slow flow parallel to the line of centres of two spheres spaced twenty diameters apart. The exact solution of Stimson & Jeffery (1926), using spherical bipolar co-ordinates, shows that the drag on each sphere deviates by nearly 5 % from the drag for a single isolated sphere even at this distance. This deviation is rather remarkable when one considers that the solid angle subtended by the boundary of the second sphere is only 1/1600 of the total solid angle. Consider next the continuous distribution of disturbances representing an extended shape. Batchelor (1970) estimates that the error in drag due to end effects in slender-body creeping-motion theory is given by $\epsilon = (0{\cdot}69 + 2{\cdot}30n)^{-1}$, where $L/R = 10^n$; thus a 10 % error in drag can be anticipated for objects with aspect ratios as large as $10^4$.

The long-range effects just described make it impractical in general to handle infinite-domain Stokes-like flows using numerical finite-difference schemes with finite but large integration domains. Similarly, solution techniques based on iterative procedures, such as the method of reflexions (see Happel & Brenner (1965) for an excellent summary of the applications of this solution procedure), which are highly successful for dilute systems, are very slowly convergent when disturbances are closely spaced or continuously distributed. As an illustration,

the first nine terms of the Faxen (1925) series solution for the flow parallel to the axis of two touching spheres, using this method, yield drag results that deviate by about 25% from the Stimson & Jeffery (1926) exact solution. One therefore seeks a method of solution which is particularly suited for treating flows with slowly decaying disturbances. One such method, which has been applied with considerable success in potential-flow theory (see Hess & Smith (1966) for summary), is the so-called boundary method. In this method one does not solve directly for the flow field in all of space, but seeks to determine instead that unknown distribution of fundamental singular solutions of the governing differential equation which will enable the requisite boundary condition to be satisfied on the object surface. The method applies to any linear boundary-value problem, and has the advantage that it effectively reduces the number of dimensions over which the unknown functions need to be determined, provided the singular solutions representing the desired boundaries can be distributed either over a surface, a line or at discrete points. For surface distributions of singularities one has to solve a one- or two-dimensional integral equation, depending on whether the object is two-dimensional, axially symmetric or truly three-dimensional, while for discrete point distributions one has to solve an array of linear algebraic relations. The disadvantages of the boundary method are that the derivation of the fundamental singular solution, its spatial distribution and completeness for satisfying a given boundary-value problem can be very difficult to find. The discussion of the next few paragraphs will elucidate these remarks.

Some basic insight into the above problems for the Stokes flow can be deduced from the known results of the simpler, related problem for potential flow. These potential-flow results have the further importance that they are derived for Laplace's equation, for which mathematically rigorous statements about uniqueness and related questions are known to be true. Basic works on potential-flow theory (e.g. Kellogg 1929) show that the disturbance potential of an object can under quite general conditions be represented by a source distribution over its surface. The point source thus serves as the kernel in the integral equation for the general three-dimensional body. The principal limitation is that the representation does not apply in the immediate vicinity of discontinuous changes in body slope. For two-dimensional flow this representation is formally equivalent to a surface vorticity distribution (Praeger 1928), and for axially symmetric flow to a surface distribution of constant strength ring sources (Vandrey 1964; Hess & Smith 1966). For certain special geometries, surface source or vortex distributions do not appear to be necessary, but can be replaced by a point singularity (sphere) or a line distribution of internal sources which can be finite (prolate spheroid) or infinite (two-dimensional circular cylinder) in length. Internal line source distributions also provide the basis for the approximate representations introduced by von Kármán (1930), and used by numerous investigators in slender-body potential-flow theory, where the line source distributions are located along the axis of symmetry. This simple internal distribution cannot be used to represent an arbitrary axisymmetric body; for there is no assurance that a potential function, which is analytic outside a closed boundary, can be continued analytically to the axis without encountering

singularities. This same argument of course applies to any higher-order distribution of internal singularities, although for potential flow the singularities considered in the literature have been confined, to the authors' knowledge, to source, dipole or vortex distributions. Higher-order internal distributions, however, have recently been applied to varied problems in the Stokes flow, and these results will be discussed shortly.

In contrast to potential-flow theory, the problem of the derivation and distribution of fundamental singular solutions for the three-dimensional Stokes flows has not been resolved, except for special geometries where the boundaries conform to a co-ordinate surface of one of the orthogonal co-ordinate systems for which the generalized axisymmetric Stokes flow equation is simply separable. For the latter geometries, Payne & Pell (1960) have shown that the infinite set of simply separable singular solutions for each co-ordinate system provides a complete set of generating functions, which can be used to satisfy rather general viscous-flow boundary conditions along any constant co-ordinate surface of the same orthogonal co-ordinate system. Wang & Skalak (1969), Chen & Skalak (1970) and Gluckman *et al.* (1971) have taken advantage of the completeness of these fundamental separable solutions to obtain the exact Stokes solutions for both the infinite periodic and finite line arrays of spheres and spheroids referred to earlier. In these studies, a single infinite sequence of appropriate singularities is placed at the origin of each sphere and spheroid. The results of Gluckman *et al.* (1971) are of further interest in that they include a detailed investigation of the convergence properties for the Stokes flow of a variation of the boundary method for multiparticle flow termed the multipole truncation technique. The convergence tests for the technique show that for closely spaced simple objects it is far more efficient to use a truncated series of point singularities, and satisfy boundary conditions at discrete points on each object simultaneously, than to generate a series solution through successive iteration in which an approximate boundary-value problem is solved exactly at each order, as in the method of reflexions. For example, the multipole truncation technique yields first-, second- and fifth-order truncation solutions for the drag, which are accurate to 2·5, 0·1 and 0·001 % respectively for the flow parallel to the axis of two touching spheres. This rapid convergence of the solution for the drag is in sharp contrast to the previously mentioned results obtained by Faxen (1925) using the method of reflexions.

While the infinite sequence of simple separable solutions placed at the origin of a given orthogonal co-ordinate system is a complete set of functions for only a constant co-ordinate surface of that same orthogonal co-ordinate system, this does not preclude its careful use as an approximate representation for other boundaries. For example, O'Brien (1968) and Hyman (1970) have obtained good numerical approximations for slightly deformed spheres using a truncated set of separable spherical solutions placed at the centre of each object. This same type of approximate representation was also examined by the authors for axially symmetric objects with greater eccentricity than those considered by O'Brien and Hyman prior to the development of the general formulation presented herein. Several numerical experiments were performed, in which different

distributions of internal spherical singularities were used to approximate prolate spheroids of various aspect ratios. These results are summarized briefly in appendix A. Good numerical agreement with exact solutions could only be obtained for prolate spheroids with aspect ratios less than 1·5. Furthermore, for a prolate spheroid with an aspect ratio of 2, the numerical solutions did not converge as the number of higher order spherical multipoles† retained in the description was increased (see tables 6 and 7). Approximate representations using a continuous line distribution of the lowest-order spherical singularity, the point force, have also been extensively studied. This approximation forms the basis for the various investigations of the slender-body Stokes flow mentioned previously.

Tuck (1968) and Batchelor (1970) suggest that a suitable axial distribution of singularities might be used to represent arbitrary (not necessarily slender) axisymmetric bodies, but do not exploit this idea further. Both authors are careful to point out that the validity of the approach for non-slender shapes depends critically on whether the exact solution for the external flow can be continued analytically inside the body all the way to the axis.

While ingenious approximate methods might be devised for representing the more varied axisymmetric Stokes flows using judiciously chosen distributions of higher-order internal singularities, the advantage of a general formulation based on a continuous distribution of fundamental surface singularities akin to that used in potential-flow theory is self-evident.‡ The first task is to determine an appropriate fundamental singular solution. One might attempt to derive a Green's function for the generalized axisymmetric Stokes equation. However, this problem is somewhat more formidable than the equivalent two-dimensional Stokes-flow problem, where one considers the biharmonic equation and the relatively simple constant-coefficient double Laplacian operator. For this reason, the authors have adopted a more intuitive approach. In essence, one seeks to determine a fundamental ring-like singularity, which has the flexibility to satisfy viscous-flow boundary conditions on the exterior surface of a small cone frustrum of infinitesimal slant height. To this end, one notes that the fundamental separable solutions for the axisymmetric Stokes stream function, in an oblate spheroidal co-ordinate system of vanishing aspect ratio, produce a velocity disturbance which is smoothly varying everywhere except at the focal circle where both velocity components become infinite. At the surface of the vanishingly thin spheroid or disk bounded by the focal circle, a finite velocity disturbance is felt; the disk surface therefore appears as a finite source of both mass and momentum. Such a flux is of course required to balance the incident stream and satisfy the no-slip boundary conditions in the Stokes flow

† The term multipole adopted in Gluckman *et al.* (1971) refers to the superposition of the fundamental irrotational and rotational separable solutions of the same order. Thus, the lowest-order spherical multipole is the sum of a potential-flow doublet and a Stokeslet or point force. Each multipole contains two arbitrary constants, one from each solution, and provides the freedom to satisfy the viscous-flow boundary conditions at one point on the generating arc of an axisymmetric body.

‡ Tuck (1968) notes that one very important advantage of using a surface distribution of singularities is that it avoids the problem of analytic continuation inside the body.

past an actual disk. Similarly, the infinite velocity at the edge of the disk is not objectionable, since it is a singular boundary point for a real disk. On the other hand, for a general body of revolution both the singular velocity behaviour at the focal circle and the finite interior fluxes are undesirable, the first because it is incompatible with the no-slip boundary conditions on a smooth surface, the second because there can be no accumulation of mass and momentum within a closed boundary. Our objective, then, will be to derive the necessary and sufficient conditions for eliminating this unwanted behaviour. We shall find, not surprisingly, that the conditions for suppressing singular surface velocities are identical with those for eliminating interior fluxes in the plane of the singularity. It will also be shown that, except for axially perpendicular surface elements, only the two lowest-order rotational and irrotational spheroid singularities are required to satisfy viscous-flow boundary conditions on a differential surface element.

As just intimated, special treatment is required in the vicinity of surfaces perpendicular to the axis (e.g. cylinder ends or a blunt base). In the potential-flow calculations of Hess & Smith (1966), blunt surfaces did not require special treatment, while sharp edges were rounded off and represented by cone frustrums with finer dimensions. There was no need to consider singularities of an order higher than that of the ring source. In the present analysis, a similar approximation could be made, in which blunt ends would be given a slight thickness and subdivided into a fine meshwork of conical elements with steep but finite slopes. A more efficient representation, however, was discovered for surface elements perpendicular to the symmetry axis. While only the lowest-order rotational and irrotational spheroidal singularities are required to describe the uniform flow past an isolated vanishingly thin oblate spheroid or disk, the infinite array of higher-order singularities does constitute a complete set of functions to satisfy an arbitrary disturbance along the surface of the disk produced by any given distribution of other singularities in the flow field. Thus, the inclusion of higher-order spheroidal multipoles of vanishing aspect ratio placed at the axial location of a vertical portion of surface provides the freedom to satisfy the no-slip boundary conditions at any number of discrete points along this portion of surface, the number of points depending on the order of the multipoles retained in the description.

Section 2 derives the fundamental singular solution of the axisymmetric Stokes equation, which can be used to represent the disturbance produced by an infinitesimal surface element. The integral representation for a general body of revolution and its finite-difference approximation are presented in § 3. Section 4 discusses the matrix solution of the finite-difference equations, and presents results showing the convergence of the numerical solution to the exact solution for prolate spheroids as the number of approximating surface elements is increased. The use of higher-order multipoles for blunt end representations is given in § 5, together with numerical solutions presented for the flow past short finite cylinders and cones. Finally, § 6 describes an approximate method for obtaining solutions for flow past long finite cylinders using multiple prolate spheroidal representations.

## 2. The fundamental solution

As discussed in §1, the disturbance produced by complex bodies of revolution in the Stokes flow can be represented by a surface distribution of ring-like disturbances, derived as a limit process from the fundamental separable solutions of the axially symmetric equations written in oblate spheroidal co-ordinates,

$$D^2D^2\psi = 0, \tag{2.1}$$

where $\psi$ is the axially symmetric stream function, $D^2$ is the generalized axi-symmetric potential operator and $\xi$, $\eta$ are the oblate spheroidal co-ordinates shown in figure 1. They are related to the axial and radial co-ordinates $x$, $y$ by the co-ordinate transformation

$$\left.\begin{gathered} x+iy = c\sinh(\xi+i\eta), \\ x = c\sinh\xi\cos\eta, \quad y = c\cosh\xi\sin\eta, \\ c^2 = a^2-b^2. \end{gathered}\right\} \tag{2.2a}$$

The focal radii $R_1$ and $R_2$ are given by

$$R_1 = [x^2+(y-c)^2]^{\frac{1}{2}}, \quad R_2 = [x^2+(y+c)^2]^{\frac{1}{2}}. \tag{2.2b}$$

The fundamental separable solutions of (2.1), which are bounded at infinity and well behaved along the axis, were first presented by Sampson (1891).

$$\begin{aligned}\psi = {} & [D_2p+B_2H_2(p)+D_4H_4(p)]\,I_2(q)+[D_3+B_3H_3(p) \\ & +D_5H_5(p)]\,I_3(q)+\sum_{n=4}^{\infty}[D_nH_{n-2}(p)+B_nH_n(p)+D_{n+2}H_{n+2}(p)]\,I_n(q),\end{aligned} \tag{2.3}$$

where

$$p = i\sinh\xi = i\left[\left(\frac{R_1+R_2}{2c}\right)^2-1\right]^{\frac{1}{2}},$$

$$q = \cos\eta = \left[1-\left(\frac{R_2-R_1}{2c}\right)^2\right]^{\frac{1}{2}},$$

and $B_n$, $D_n$ are complex constants, $I_n(q)$ are Gegenbauer functions of the first kind, and $H_n(p)$ are Gegenbauer functions of the second kind.

For future reference $I_n$ and $H_n$ are related to the more familiar Legendre functions $P_n$ and $Q_n$, of the first and second kind, by

$$I_n = \frac{P_{n-2}-P_n}{2n-1}, \quad H_n = \frac{Q_{n-2}-Q_n}{2n-1}, \quad (n \geqslant 2), \tag{2.4}$$

where $I_0(q) = 1$, $I_1(q) = -q$, $H_0(p) = -p$, $H_1(p) = -1$.

The solutions (2.3) comprise a complete set of functions that can be used to satisfy the viscous-flow boundary conditions along a constant co-ordinate surface $p = p_0$ for an arbitrary distribution of external singularities. The total stream function is the sum of $\psi$ and all other contributions $\psi_R$ associated with the rest of the flow field. As before we are interested in the behaviour of the individual solutions (2.3) in the limit as the aspect ratio of the spheroidal co-ordinate system vanishes, that is as $b$ approaches zero and the focal radius $c$

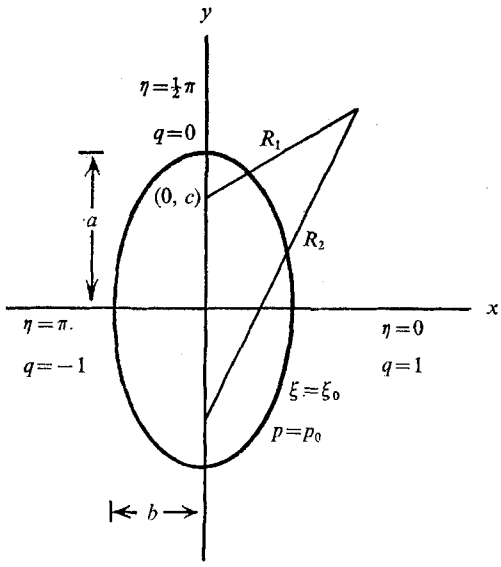


FIGURE 1. Oblate spheroidal co-ordinate system.

approaches $a$, the radius of the major axis of the spheroid. If one requires in addition that $a$ be equal to the local radius $y_s(x)$ of the generating curve of the body of revolution, the solutions (2.3) in the limit $b \to 0$ become ring-like disturbances lying on the surface of the body that is to be represented. Thus, we let $c \to y_s(x)$, denote $R_1$, $R_2$ by $\rho_1$, $\rho_2$ to indicate that the limit $b = 0$ has been taken, and express $p$, $q$ by

$$\lim_{b\to 0} p = i\left[\left(\frac{\rho_1+\rho_2}{2y_s}\right)^2 - 1\right]^{\frac{1}{2}}, \qquad \lim_{b\to 0} q = \left[1-\left(\frac{\rho_2-\rho_1}{2y_s}\right)^2\right]^{\frac{1}{2}}, \tag{2.5}$$

where, from (2.2$b$),

$$\rho_1 = [x^2+(y-y_s)^2]^{\frac{1}{2}}, \quad \rho_2 = [x^2+(y+y_s)^2]^{\frac{1}{2}}.$$

To satisfy viscous-flow boundary conditions at the surface of a general body of revolution, one needs to examine the limiting behaviour of both the $x$ and $y$ velocity components induced by the singular disturbances (2.3) as the focal ring $c = y_s$ is approached, and derive the necessary conditions for suppressing the unwanted singular behaviour. These velocity components are given by

$$u = \frac{1}{y}\frac{\partial \psi}{\partial y}, \quad v = -\frac{1}{y}\frac{\partial \psi}{\partial x}, \tag{2.6}$$

where

$$\frac{\partial \psi}{\partial x} = \frac{\partial \psi}{\partial p}\frac{\partial p}{\partial x} + \frac{\partial \psi}{\partial q}\frac{\partial q}{\partial x},$$

$$\frac{\partial \psi}{\partial y} = \frac{\partial \psi}{\partial p}\frac{\partial p}{\partial y} + \frac{\partial \psi}{\partial q}\frac{\partial q}{\partial y}.$$

While singularities of all orders are present in (2.3), we shall find that the $I_2$ and $I_3$ terms in (2.3) are sufficient by themselves to satisfy the no-slip boundary conditions to order $(\rho_1/y_s)^{\frac{1}{2}}$ on an arbitrary small surface element containing the

focal ring $c = y_s$, unless the surface element is perpendicular to the axis. Thus, truncating the expression for $\psi$ in (2.3) at $n = 3$, one has, for $\partial\psi/\partial p$ and $\partial\psi/\partial q$ in (2.6),

$$\left.\begin{aligned}\frac{\partial\psi}{\partial p} &= (D_2 - B_2 Q_1(p))\, I_2(q) - B_3 Q_2(p)\, I_3(q),\\ \frac{\partial\psi}{\partial q} &= -(D_2 p + B_2 H_2(p))\, q - (D_3 + B_3 H_3(p))\, P_2(q),\end{aligned}\right\} \tag{2.7}$$

where we have used the differentiation formulae

$$\partial I_n(q)/\partial q = -P_{n-1}(q), \quad \partial H_n(p)/\partial p = -Q_{n-1}(p).$$

The spatial derivatives of $p$ and $q$ in (2.6) are obtained from (2.5) and the associated definitions of $\rho_1$ and $\rho_2$.

$$\left.\begin{aligned}\frac{\partial p}{\partial x} &= -\frac{1}{p}\left(\frac{x}{\rho_1\rho_2}\right)\left(\frac{\rho_1+\rho_2}{2y_s}\right)^2 = -\frac{\alpha_1}{p},\\ \frac{\partial p}{\partial y} &= -\frac{1}{p}\left(\frac{\rho_1+\rho_2}{4y_s^2}\right)\left(\frac{y-y_s}{\rho_1}+\frac{y+y_s}{\rho_2}\right) = -\frac{\alpha_2}{p},\\ \frac{\partial q}{\partial x} &= \frac{1}{q}\left(\frac{x}{\rho_1\rho_2}\right)\left(\frac{\rho_2-\rho_1}{2y_s}\right)^2 = -\frac{\beta_1}{q},\\ \frac{\partial q}{\partial y} &= -\frac{1}{q}\left(\frac{\rho_2-\rho_1}{4y_s^2}\right)\left(\frac{y+y_s}{\rho_2}-\frac{y-y_s}{\rho_1}\right) = -\frac{\beta_2}{q},\end{aligned}\right\} \tag{2.8}$$

where $\alpha_{1,2}$ and $\beta_{1,2}$ are defined by (2.8). Substituting results (2.7) and (2.8) in (2.6), and using the definitions (2.4), one obtains

$$\begin{aligned}u = &-\alpha_2\left(\frac{D_2 - B_2 Q_1(p)}{2py}\right)(1-q^2) + \alpha_2\frac{B_3 Q_2(p)}{2py}\, q(1-q^2)\\ &+\frac{\beta_2}{y}(D_2 p + B_2 H_2(p)) + \frac{\beta_2}{y}(D_3 + B_3 H_3(p))\left[\frac{3q^2-1}{2q}\right],\end{aligned} \tag{2.9a}$$

$$\begin{aligned}v = &-\alpha_1\left(\frac{D_2 - B_2 Q_1(p)}{2py}\right)(1-q^2) + \alpha_1\frac{B_3 Q_2(p)}{2py}\, q(1-q^2)\\ &+\frac{\beta_1}{y}(D_2 p + B_2 H_2(p)) + \frac{\beta_1}{y}(D_3 + B_3 H_3(p))\left[\frac{3q^2-1}{2q}\right].\end{aligned} \tag{2.9b}$$

Expressions (2.9*a*, *b*) give the disturbance velocity field at any point $x$, $y$ due to the two lowest-order spheroidal multipoles of vanishing aspect ratio with a common focal ring located at $(0, y_s)$ in $x, y$ co-ordinates, and at $(0, 0)$ in $p, q$ co-ordinates. We shall now examine the behaviour of (2.9*a*, *b*) as the field point $x, y$ approaches the focal point $(0, y_s)$ along an arbitrary line $\theta$ (see figure 2(*a*)) in a meridian plane containing the symmetry axis.

The functions $Q_1$, $Q_2$, $H_2$, $H_3$ are infinite series which converge for $|p| \leqslant 1$. As $p \to 0$ these infinite series can be approximated by

$$\left.\begin{aligned}Q_1(p) &= -1 + p^2 + O(p^4), \quad Q_2(p) = -2p + \tfrac{4}{3}p^3 + O(p^5),\\ H_2(p) &= p - \tfrac{1}{3}p^3 + O(p^5), \quad H_3(p) = -\tfrac{1}{3} + p^2 + O(p^4).\end{aligned}\right\} \tag{2.10}$$

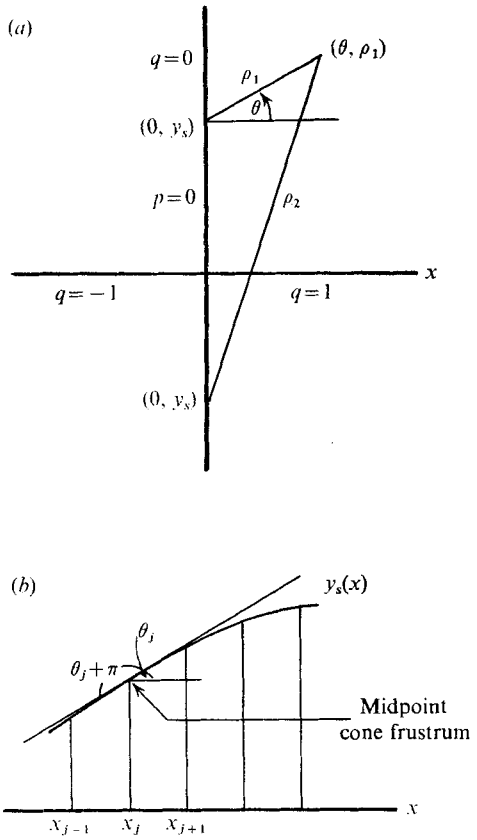


FIGURE 2. (*a*) Geometry of an oblate spheroid of zero aspect ratio. (*b*) Piecewise representation of a section of a general body of revolution.

Since the $\alpha_i$ and $\beta_i$ are of $O(1)$ except as $\theta \to \frac{1}{2}\pi$ (see (2.14)), a cursory examination of (2.9*a*, *b*) and (2.10) shows that both $u$ and $v$ in (2.9) become singular in the limit $p \to 0$, $q \to 0$. Such singular behaviour is, of course, incompatible with satisfying no-slip boundary conditions at a solid surface, and must be eliminated. The necessary conditions for suppressing this unwanted behaviour can be deduced by developing $u$ and $v$ in (2.9*a*) and (2.9*b*) as a Taylor series expansion about $p = 0$, $q = 0$. We shall find that consideration of the lowest-order terms in this Taylor series expansion is sufficient for eliminating the singular velocities, but does not lead to a unique determination of the complex constant coefficients. One must proceed to the next higher-order terms in the series to see how these coefficients are uniquely determined by the no-slip boundary conditions.

Referring to figure 2(*a*), one observes from the geometry that

$$\rho_2^2 = (2y_s + \rho_1 \sin\theta)^2 + \rho_1^2 \cos^2\theta. \tag{2.11}$$

Now, provided $y_s \neq 0$, there will always be some small neighbourhood about the focal point in the upper half of the meridian plane $(0, y_s)$ where (2.11) can be approximated by

$$\rho_2 = 2y_s\left(1 + \frac{\rho_1}{2y_s}\sin\theta + O\left(\frac{\rho_1}{y_s}\right)^2\right). \tag{2.12}$$

Substituting (2.12) into (2.5) one finds that both $p$ and $q$ can be developed as an infinite series in fractional half powers of $\rho_1/y_s$:

$$p = i\left[\left(\frac{\rho_1}{y_s}\right)^{\frac{1}{2}}\pi_1 + O\left(\frac{\rho_1}{y_s}\right)^{\frac{3}{2}}\right], \quad q = \left(\frac{\rho_1}{y_s}\right)^{\frac{1}{2}}\pi_2 + O\left(\frac{\rho_1}{y_s}\right)^{\frac{3}{2}}, \tag{2.13}$$

where $\pi_1 = (1+\sin\theta)^{\frac{1}{2}}$, $\pi_2 = (1-\sin\theta)^{\frac{1}{2}}$. Similarly, the $\alpha_i$ and $\beta_i$ in (2.9) from their definitions in (2.8) can with the aid of (2.12) be written as

$$\left.\begin{aligned} \alpha_1 &= \frac{\cos\theta}{2y_s} + O\left(\frac{\rho_1}{y_s}\right), \quad \alpha_2 = \frac{1+\sin\theta}{2y_s} + O\left(\frac{\rho_1}{y_s}\right), \\ \beta_1 &= -\frac{\cos\theta}{2y_s} + O\left(\frac{\rho_1}{y_s}\right), \quad \beta_2 = \frac{1-\sin\theta}{2y_s} + O\left(\frac{\rho_1}{y_s}\right). \end{aligned}\right\} \tag{2.14}$$

The Taylor series expansion of $u$ and $v$ about the focal point $(0, y_s)$ is now readily obtained by substituting results (2.10), (2.13) and (2.14) in (2.9). Both series are in fractional half powers of $\rho_1/y_s$ and take the form

$$\left.\begin{aligned} u &= u_1\left(\frac{\rho_1}{y_s}\right)^{-\frac{1}{2}} + u_2\left(\frac{\rho_1}{y_s}\right)^{\frac{1}{2}} + O\left(\frac{\rho_1}{y_s}\right)^{\frac{3}{2}}, \\ v &= v_1\left(\frac{\rho_1}{y_s}\right)^{-\frac{1}{2}} + v_2\left(\frac{\rho_1}{y_s}\right)^{\frac{1}{2}} + O\left(\frac{\rho_1}{y_s}\right)^{\frac{3}{2}}, \end{aligned}\right\} \tag{2.15}$$

where the $u_i$ and $v_i$ are of order unity except as $\theta \to \frac{1}{2}\pi$. The expressions for $u_1$ and $v_1$ in (2.15) are given by

$$\left.\begin{aligned} u_1 &= \frac{i\pi_1}{4y_s^2}(D_2+B_2) - \frac{\pi_2}{4y_s^2}\left(D_3 - \frac{B_3}{3}\right), \\ v_1 &= \frac{i\cos\theta}{4y_s^2\pi_1}(D_2+B_2) + \frac{\cos\theta}{4y_s^2\pi_2}\left(D_3 - \frac{B_3}{3}\right). \end{aligned}\right\} \tag{2.16}$$

It is evident from (2.15) that if $u$ and $v$ are not to be singular as $\rho_1 \to 0$ on an arbitrary line passing through the focal point $(0, y_s)$ then both $u_1$ and $v_1$ must vanish for all $\theta$. Thus, from (2.16), the singular behaviour can be suppressed by requiring the coefficients of the rotational and irrotational solutions to satisfy the compatibility conditions

$$D_2 = -B_2, \quad D_3 = \tfrac{1}{3}B_3. \tag{2.17}$$

No further information can be obtained from the leading terms in the expansion (2.15), and one must proceed to the next term in the expansion to see how the no-slip boundary conditions are satisfied on a small surface element in the vicinity of the focal circle.

The expressions for $u_2$ and $v_2$ in (2.15) obtained from (2.9), (2.10), (2.13) and (2.14) are quite lengthy, but simplify significantly once the coefficient relations (2.17) are used. These simplified expressions are

$$\left.\begin{aligned} u_2 &= \frac{i\pi_1^3}{4y_s^2}B_2 - \frac{\pi_1^2\pi_2}{4y_s^2}B_3, \\ v_2 &= \frac{i\pi_1\cos\theta}{4y_s^2}B_2 - \frac{\cos\theta}{4y_s^2}\left(2\pi_2 + \frac{\pi_1^2}{\pi_2}\right)B_3. \end{aligned}\right\} \tag{2.18}$$

Equation (2.15) with $u_1 = v_1 = 0$ and $u_2$, $v_2$ given by (2.18) is smoothly behaved and describes the local disturbance produced by an isolated spheroidal singularity in the vicinity of its focal circle. To see how this isolated disturbance enters into the problem of satisfying viscous boundary conditions on a general body of revolution one must consider the disturbance velocities $u_R$ and $v_R$ produced by all other disturbances in the flow field. In the local region for which the Taylor series expansion (2.15) is valid, $u_R$ and $v_R$ are smoothly varying functions. In essence then, one would like to determine the $B_2$ and $B_3$ coefficients in (2.18) by requiring that the $u_2$ and $v_2$ terms in (2.15) negate locally the $u_R$ and $v_R$ contributions, and thereby satisfy the no-slip boundary conditions in some mean sense on an arbitrary cone frustrum of small slant height whose midpoint is the focal circle of the disturbance (2.9) or its local representation (2.15).

As shown in figure 2(*b*), the general body of revolution is approximated by a piecewise continuous sequence of $j = 1, 2, \ldots, N$ frustrums of cones, which in the limit of vanishing slant height $N \to \infty$ will exactly represent the body. A ring-like disturbance given by (2.9), now denoted by $u_j$ and $v_j$ to distinguish the $j$th surface element with local behaviour described by (2.15), is placed in the surface at the midpoint of each conical element. The slope of the $j$th surface is $\tan\theta_j$ and its length is given by $2l_j$. $u_{Rj}$ and $v_{Rj}$ now denote the disturbance velocity due to all disturbances not located in the $j$th element. Thus, to satisfy the no-slip boundary conditions in an integral average sense on the $j$th surface element one requires that

$$\left.\begin{aligned} 0 &= \int_{-l_j}^{0} u_{Rj} + u_j(\rho_{1j}, \pi+\theta_j)\, d\rho_{1j} + \int_{0}^{l_j} u_{Rj} + u_j(\rho_{1j}, \theta_j)\, d\rho_{1j}, \\ 0 &= \int_{-l_j}^{0} v_{Rj} + v_j(\rho_{1j}, \pi+\theta_j)\, d\rho_{1j} + \int_{0}^{l_j} v_{Rj} + v_j(\rho_{1j}, \theta_j)\, d\rho_{1j}. \end{aligned}\right\} \tag{2.19}$$

The range of integration in (2.19) has been split about the midpoint of the element, since the functions $u_{2j}$ and $v_{2j}$ in (2.18) change in passing through the focal point from the third to the first quadrant. The surface element whose angle is $\theta_j$ in the first quadrant is $\pi+\theta_j$ in the third quadrant. One observes from (2.13) that $\pi_1(\theta_j+\pi) = \pi_2(\theta_j)$ and that $\pi_2(\theta_j+\pi) = \pi_1(\theta_j)$. Thus, in the third quadrant $u_{2j}$ and $v_{2j}$ from (2.18) are given by

$$\left.\begin{aligned} u_{2j} &= \frac{i\pi_2^3}{4y_s^2} B_{2j} - \frac{\pi_1\pi_2^2}{4y_s^2} B_{3j}, \\ v_{2j} &= \frac{-i\pi_2 \cos\theta_j}{4y_s^2} B_{2j} + \frac{\cos\theta_j}{4y_s^2}\left(2\pi_1 + \frac{\pi_2^2}{\pi_1}\right) B_{3j}. \end{aligned}\right\} \tag{2.20}$$

The integration of (2.19) using relations (2.15), (2.18) and (2.20) is straightforward. We give only the final result truncated at $O(l_j/y_s)^{\frac{3}{2}}$:

$$6y_s\left(\frac{y_s}{l_j}\right)^{\frac{3}{2}} \int_{-l_j}^{l_j} u_{Rj}\, d\rho_{1j} = -i(\pi_1^3 + \pi_2^3)\, B_{2j} + \pi_1\pi_2(\pi_1+\pi_2)\, B_{3j}, \tag{2.21a}$$

$$\frac{6y_s}{\cos\theta_j}\left(\frac{y_s}{l_j}\right)^{\frac{3}{2}} \int_{-l_j}^{l_j} v_{Rj}\, d\rho_{1j} = i(\pi_2-\pi_1)\, B_{2j} + \left[2(\pi_2-\pi_1) + \frac{\pi_1^2}{\pi_2} - \frac{\pi_2^2}{\pi_1}\right] B_{3j}. \tag{2.21b}$$

The integrals on the left-hand side of (2.21) are well-behaved functions, in which all the other $B_{2i}$ and $B_{3i}$ ($i \neq j$) appear linearly owing to the linear summation of disturbances. Thus (2.21*a*) and (2.21*b*) provide two linearly independent equations for $B_{2j}$ and $B_{3j}$ in terms of all the other coefficients and the incident stream. In general, for a body of revolution approximated by $N$ conical elements one obtains a coupled system of $2N$ linear algebraic relations for the $B_{2j}$ and $B_{3j}$ ($j = 1, 2, \ldots, N$) which can be solved by a suitable matrix inversion technique. In the limit as $N \to \infty$, $l_j \to dl_j$, the $B_{2j}$ and $B_{3j}$ become a continuous distribution $B_2(x)$ and $B_3(x)$ and the no-slip boundary conditions are satisfied in an integral average sense on each differential surface element $dl_j$. The matrix of equations (2.21) ($j = 1, 2, 3, \ldots, N$) have a unique solution provided none of the $\theta_j = \frac{1}{2}\pi$. This case, which is exceptional because the integral term on the left-hand side of (2.21*b*) becomes infinite, is given special consideration in § 5.

We now return to the question as to why the higher-order separable solutions with coefficients $n \geqslant 4$ in (2.3) can be omitted in the representation of a piecewise smooth body of revolution whose local slope is nowhere perpendicular to the axis. In general all the higher-order $B_{nj}$ and $D_{nj}$ are determined by requiring that the no-slip boundary conditions be satisfied to higher order in the Taylor expansion (2.15). The boundary-value problem for each higher-order term in the expansion introduces $2N$ new algebraic relations which are obtained in the same manner as (2.21*a*) and (2.21*b*). Similarly, each higher-order multipole in (2.3) provides $2N$ new coefficients and thus the freedom to satisfy the $2N$ additional relations. In the limit as $l_j \to dlj$ the spheroidal solutions with coefficients $n \geqslant 4$ provide only higher-order differential corrections which can be neglected in a superposition integral based on a continuous distribution of surface singularities. These high-order spheroidal solutions could be used to provide improved accuracy for a numerical approximation in which the body is represented by $N$ frustrums of cones, but here again the same improved accuracy could just as easily be obtained by increasing $N$, the number of approximating surface elements.

From the foregoing derivations and discussions, it is reasonable to construct the fundamental solution for the stream function for an arbitrary convex body of revolution from only the two lowest-order rotational and irrotational spheroidal singularities in (2.3),

$$\chi = B_2(-p + H_2(p))\, I_2(q) + B_3(\tfrac{1}{3} + H_3(p))\, I_3(q), \tag{2.22}$$

where the limit process indicated by equations (2.5) has been applied and the compatibility conditions (2.17) satisfied.

In concluding § 2 we inquire whether the fundamental solution just derived might have a simple physical description. To this end we examine the behaviour of the fundamental solution (2.22) in the plane $x = 0$. On first glance it might appear that the disturbance in this plane is disk-like rather than ring-like in nature. This behaviour is suggested by the fact that the solution for the axisymmetric flow past an isolated disk is described by just the $B_2$ and $D_2$ terms in (2.3) in the limit $b = 0$. For a uniform incident stream this disk solution is given by

$$\psi = 2y_s^2 U I_2(q)\left[I_2(p) - \frac{p + H_2(p)}{2p_0}\right], \tag{2.23}$$

where the first term is the free-stream contribution $\psi_\infty$ and $p_0 \to 0$ is the disk surface.

Let us now compare the behaviour of solutions (2.22) and (2.23) in the plane $x = 0$. From (2.5), when $x = 0$, $q = 0$ for $y > y_s$ and $q^2 = 1-(y/y_s)^2$ for $y < y_s$. Thus, when $x = 0$, $I_2(q) = \frac{1}{2}$ for $y > y_s$, while $I_2(q) = \frac{1}{2}(y/y_s)^2$ for $y < y_s$, which is the same $y$ dependence as for a uniform stream. As $p = p_0 \to 0$, the second term in brackets in (2.23) has the limiting value $\frac{1}{2}$ and, as one would expect, just cancels the free-stream contribution along the disk surface since $I_2(0) = \frac{1}{2}$. The $B_2$ and $D_2$ terms in the disk solution therefore act just as a uniform axial source of momentum emanating at the disk surface. By contrast, the $p$ dependence in both the $B_2$ and $B_3$ terms in (2.22) vanishes as $p \to 0$. The coefficient relations (2.17) are therefore the necessary and sufficient conditions for the elimination of the axial flow in the interior of the focal circle. On the other hand, for $x = 0$ and $y > y_s$ a finite axial velocity exists. This axial flow arises solely from the $B_2$ term in (2.22) since $I_3(q) = 0$ for $x = 0$ and $y > y_s$. In the vicinity of the focal circle the axial velocity component is approximated by (2.15) with $u_1 = 0$ and $u_2$ given by (2.18) evaluated at $\theta = \frac{1}{2}\pi$.

In a similar manner the radial velocity in the plane of the focal circle can be examined. One finds that $v = 0$ everywhere in the plane $x = 0$ for the disk solution (2.23), whereas $v = 0$ only for $y < y_s$ for the fundamental disturbance (2.22). For $y > y_s$ there is a finite contribution to the radial velocity along $x = 0$ that arises now from the $B_3$ term in (2.22). The function $I_3(q)$ is a bilobular disturbance with zeros at $q = 0, \pm 1$ and a maximum at $q = 1/\sqrt{3}, -1/\sqrt{3}$ in that order. The streamline pattern for the fundamental disturbance (2.22) is therefore comprised of two ring vortices rotating in an opposite sense with a stagnation ring at the focal circle. The strength of the vortices, and hence their orientation with respect to the axis, is determined by the relative magnitude of the $B_2$ and $B_3$ coefficients.

## 3. The superposition integral and its numerical representation

One would now like to construct a superposition integral representing a general body of revolution from the fundamental disturbance derived in §2. From (2.22) the kernel of this superposition integral is

$$\chi(x, y : x', y_s(x')) = B_2(x')\,[H_2(p) - p]\,\tfrac{1}{2}(1-q^2) + B_3(x')\,[H_3(p) - \tfrac{1}{3}]\,\tfrac{1}{2}q(1-q^2), \quad (3.1)$$

where

$$p = p(x, y : x', y_s(x')) = i\left[\left(\frac{\rho_1+\rho_2}{2y_s(x')}\right)^2 - 1\right]^{\frac{1}{2}},$$

$$q = q(x, y : x', y_s(x')) = \left[1 - \left(\frac{\rho_2-\rho_1}{2y_s(x')}\right)^2\right]^{\frac{1}{2}},$$

$$\rho_1 = \rho_1(x, y : x', y_s(x')) = [(x-x')^2 + (y-y_s(x'))^2]^{\frac{1}{2}},$$

$$\rho_2 = \rho_2(x, y : x', y_s(x')) = [(x-x')^2 + (y+y_s(x'))^2]^{\frac{1}{2}}.$$

Here $x, y$ is an arbitrary field point, $x', y_s(x')$ are the co-ordinates of the focal circle of the elemental ring like disturbance and $B_2(x')$ and $B_3(x')$ are the strength

per unit length of the two lowest order multipoles at $x'$. The total stream function $\Psi$ is then the summation of $\psi_\infty$, the stream function for the incident stream, and a superposition integral representing the summation of all surface disturbances on a body of length $l$.

$$\Psi = \psi_\infty + \int_0^l B_2(x')\,[H_2(p)-p]\,\tfrac{1}{2}(1-q^2) + B_3(x')\,[H_3(p)-\tfrac{1}{3}]\,\tfrac{1}{2}q(1-q^2)\,dx'. \quad (3.2)$$

The unknown distributions $B_2(x')$ and $B_3(x')$ are determined by requiring that $u$ and $v$, hence $\partial\Psi/\partial x$ and $\partial\Psi/\partial y$ satisfy appropriate boundary conditions along $y_s(x)$, the surface of the body. The integral equations for $B_2(x')$ and $B_3(x')$ are therefore obtained by differentiating (3.2) using results (2.6) and (2.7) and applying the no-slip boundary conditions on $y_s(x)$:

$$\frac{\partial\psi_\infty}{\partial x} = \int_0^l \frac{B_2(x')}{2}\left[\frac{\partial p}{\partial x}(Q_1(p)+1)(1-q^2) + 2\frac{\partial q}{\partial x}(H_2(p)-p)\,q\right] + \frac{B_3(x')}{2}\left[\frac{\partial p}{\partial x}(Q_2(p)+\tfrac{1}{3})(q-q^3) - \frac{\partial q}{\partial x}(H_3(p)-\tfrac{1}{3})(1-3q^2)\right]dx', \quad (3.3)$$

$$\frac{\partial\psi_\infty}{\partial y} = \int_0^l \frac{B_2(x')}{2}\left[\frac{\partial p}{\partial y}(Q_1(p)+1)(1-q^2) + 2\frac{\partial q}{\partial y}(H_2(p)-p)\,q\right] + \frac{B_3(x')}{2}\left[\frac{\partial p}{\partial y}(Q_2(p)+\tfrac{1}{3})(q-q^3) - \frac{\partial q}{\partial y}(H_3(p)-\tfrac{1}{3})(1-3q^2)\right]dx'. \quad (3.4)$$

The integrals in (3.3) and (3.4) are evaluated at each point along the profile curve of the body by letting the field point $x, y$ in the expressions for $p$ and $q$ in (3.1) be a specified point on the surface. The expressions for $\partial p/\partial x$, $\partial p/\partial y$, $\partial q/\partial x$, $\partial q/\partial y$ are given by (2.8) with $x$ replaced by $x-x'$. The solutions of (3.3) and (3.4) for the disturbance distributions $B_2(x')$ and $B_3(x')$ when substituted back in (3.2) provide the solution for the entire flow field. For reasons given earlier, the formulation of the boundary-value problem as a coupled pair of integral equations (3.3) and (3.4) has the important advantage that it has reduced the task of obtaining a solution from that of determining an unknown function in all of space to that of determining a one-dimensional distribution of unknown coefficients for an elemental disturbance whose functional form is known.

The solution of (3.3) and (3.4) for a general boundary shape is not possible analytically, but is readily accomplished by finite-difference methods. As described in § 2 and shown in figure 2 (*b*), a general body of revolution can be formed from $j = 1, 2, \ldots, N$ contiguous surface elements each of which is the frustrum of a cone. To satisfy the no-slip boundary conditions at any convenient point on the line segment used as the generating arc for each conical element, $B_2(x)$ and $B_3(x)$ in the integrand of (3.3) and (3.4) are approximated by different but constant values for each cone frustrum. The latter is equivalent to placing a finite number of constant strength ring-like disturbances at suitably chosen intervals along the surface of the object. The integration of (3.3) and (3.4) yields two linear algebraic relations for each cone frustrum. Consequently, a system of $2N$ linear algebraic equations for the $2N$ unknown $B_{2j}$ and $B_{3j}$ is obtained for the entire surface.

In accord with the remarks of the last paragraph, (3.3) can be approximated numerically at any point $x, y_s(x)$ on the profile curve of the body by

$$\frac{\partial \psi_\infty}{\partial x} = \sum_{j=1}^{N} \frac{B_{2j}}{2} \int_{-l_j \cos\theta_j}^{l_j \cos\theta_j} \left[ \frac{\partial p}{\partial x} (Q_1(p)+1)(1-q^2) + 2\frac{\partial q}{\partial x}(H_2(p)-p)q \right] dx_j$$
$$+ \frac{B_{3j}}{2} \int_{-l_j \cos\theta_j}^{l_j \cos\theta_j} \left[ \frac{\partial p}{\partial x} (Q_2(p)+\tfrac{1}{3})(q-q^3) - \frac{\partial q}{\partial x}(H_3(p)-\tfrac{1}{3})(1-3q^2) \right] dx_j, \quad (3.5)$$

where the integration is now performed separately over each axial line segment of length $2l_j \cos\theta_j$ representing the axial projection of the generating curve for each conical element and then summed over all such segments. A related expression may be obtained from (3.4).

Although the kernels of the integrals in (3.5) are smoothly behaved, since the singular behaviour of the velocity components at the surface has been suppressed, the kernel still becomes a sensitive function of position as the integration approaches the axial station $x$ at which the no-slip boundary condition is to be satisfied. Therefore, it is convenient to use two different approximations in evaluating the integrals in (3.5), depending on whether the boundary point lies inside or outside the range of integration of the $j$th surface element. (Note that each integral gives a result equivalent to (2.21) where the disturbances are distributed at discrete locations $x = x_j$ and the no-slip boundary conditions satisfied in an integral average sense on each surface element. Here the disturbances are continuously distributed, and the no-slip boundary conditions satisfied at discrete points along the profile curve of the body.)

When the boundary point at which the no-slip boundary condition is to be satisfied lies inside the $j$th integration interval the kernel in (3.5) is approximated by the lowest-order non-vanishing term of its Taylor series expansion about this boundary point. This series, except for multiplicative constants, is obviously the same as (2.15). Thus, if the boundary points at which (3.5) is satisfied in the $j$th integration interval is at $x_j = 0$, the centre of the generating line segment for the $j$th cone frustrum, the integration of (3.5) in this interval yields the right-hand side of (2.21*a*) with an appropriate multiplicative factor. When the boundary point at which the no-slip boundary condition is to be satisfied lies outside the $j$th integration interval, the kernel in (3.5) will be a slowly-varying function over the range of integration for each surface element. A satisfactory approximation in this case is to simply treat the kernel as a constant, whose value is given by its value at the centre of the interval. The final result obtained by integrating (3.5) in the manner just described, and the related expression derived from (3.4) are given in appendix B. Equations (B1) and (B2) provide $2N$ linearly independent equations for the $B_{2j}$ and $B_{3j}$. These equations have a unique solution provided none of the $\theta_j = \frac{1}{2}\pi$.

The drag force exerted by the fluid on the body is readily computed using a technique developed by Payne & Pell (1960). These authors show that the drag force $F$ on an isolated spheroid in an incident stream is given by

$$F = 8\pi\mu \lim_{R\to\infty} \frac{(\Psi - \psi_\infty)}{R \sin^2\phi}, \quad (3.6)$$

where $R$ and $\phi$ are the distance and polar angle using the centre of the spheroid as the origin. In Gluckman *et al.* (1971) it is shown that evaluation of (3.6) for any co-axial distribution of spheroids leads to

$$F_j = \frac{4\pi\mu D_{2j}}{c_j} \tag{3.7}$$

for the drag on the $j$th spheroid. The drag is therefore determined by the coefficient of only the lowest-order rotational solution in (2.3), however, the value of $D_{2j}$ depends implicitly on all terms in the expression for $\Psi$, since it is just one element in the set of matrix equations for the coefficients.

The expression for the drag on a general body of revolution whose stream function is given by (3.2) is readily deduced from (3.7). In the limit as the aspect ratio of the spheroid vanishes $b_j \to 0$, $c_j \to y_s(x)$ and

$$F = \int_0^l \frac{4\pi\mu D_2(x)}{y_s(x)}\, dx, \tag{3.8}$$

where $D_2(x)$ is the disturbance intensity per unit length of the lowest-order rotational component of the fundamental solution.

## 4. Convergence to exact solution for prolate spheroid

In obtaining the numerical results presented here, the authors chose the more expedient path of adapting for present needs the computer program already developed in Gluckman *et al.* (1971) for axisymmetric flow past multiple oblate spheroids rather than writing and debugging a new program based on equations (B1), (B2). The similarity between using a finite number of singularities applied at discrete locations and dividing a continuous distribution into a finite number of uniform strength subdistributions has already been discussed. The multiple spheroid program used in Gluckman *et al.* has the flexibility for handling an arbitrary arrangement of fundamental separable oblate spheroidal solutions (2.3) with small but non-vanishing aspect ratio distributed at discrete points along a common axis. With this restriction, one cannot use the continuous distribution of fundamental solutions (3.1) for which $b = 0$, but has to approximate the kernel of the integral (3.2), and consequently (3.3) and (3.4), by a discrete point distribution of low aspect ratio oblate spheroidal singularities with touching $p = p_0$ co-ordinate surfaces. Again, only the two lowest-order spheroidal multipoles are required, however: the simple compatibility relations (2.17) are no longer exact, and the ring-like disturbances emanating at the focal circle now lie some small distance below the surface. As discussed in Gluckman *et al.*, conditions (2.17) can be replaced with the requirement that the no-slip boundary conditions do not lead to a matrix equation for the $B_{2,3j}$ and $D_{2,3j}$ which is ill-conditioned as one approaches the apex $\theta_j = \frac{1}{2}\pi$ of the inscribed spheroids. The latter is accomplished numerically by satisfying the no-slip boundary conditions at two symmetrically distributed points in the profile curve in close proximity to, rather than exactly at, $\theta_j = \frac{1}{2}\pi$. In this manner, singular velocities are suppressed as one approaches the profile curve of the body

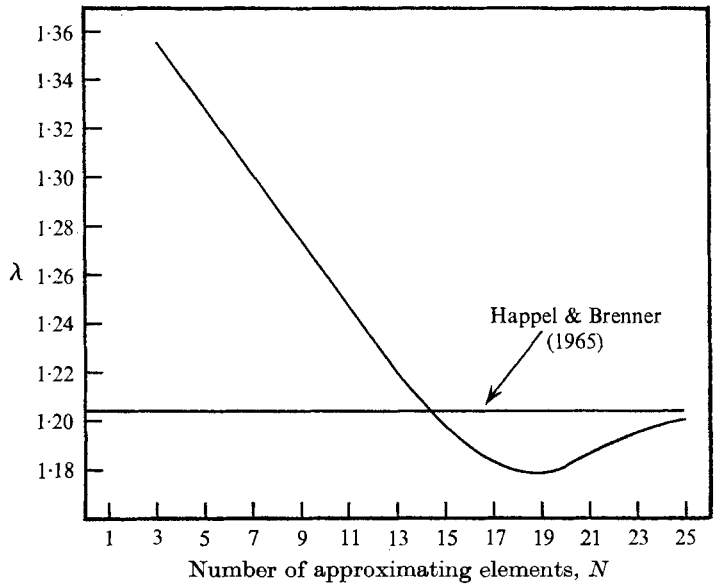


FIGURE 3. Drag correction factor $\lambda$ for a prolate spheroid of aspect ratio = 2·0 using $N$ boundary points with equal axial spacing.

and a matrix equation obtained for the coefficients, which is equivalent in all other respects to (B1) and (B2).

In order to demonstrate the convergence characteristics of this computational procedure for representing axisymmetric bodies of arbitrary shape, a prolate spheroid of aspect ratio 2·0 was selected, and sample drag calculations performed for an increasing number of approximating surface elements. This aspect ratio was chosen as it is too large to be represented by a converging sequence of spherical multipoles (see appendix A), and is small enough to require a reasonable number of oblate spheroidal singularities for convergence without consuming excessive amounts of computer time. Following the convention of Happel & Brenner, the drag on a prolate spheroid can be written as

$$F = 6\pi\mu U r_n \lambda,$$

where $r_n$ is the minor radius of the spheroid and $\lambda$ is a correction factor representing the ratio of the drag on the spheroid to the drag on a sphere with the same projected area as the spheroid in a plane perpendicular to the stream direction. Drag correction factors $\lambda$ were calculated using oblate spheroidal singularities distributed at from 3 to 25 equally spaced stations along the axis of the prolate spheroid. Only the two lowest-order oblate spheroidal multipoles were used for each element, except the two end elements, where the first four multipoles in the series were used to obtain a more accurate representation of the spheroidal ends. The results of this experiment are shown in figure 3, which is a plot of the drag correction factor $\lambda$ as a function of the number of discrete point elements used for the representation. If only three elements are employed, the error in $\lambda$ is 12·5 %, whereas if a 25-point distribution is used the solution approaches the exact solution asymptotically with a local error of less than 0·4 %.

As will be evident from the results of § 5, the relatively slow convergence to the exact solution is due to the difficulty in obtaining accurate end representations for surface elements nearly perpendicular to the axis unless very low aspect ratio spheroidal singularities are used.

## 5. Objects with axially perpendicular surface elements

The linear matrix of equations for the $B_{2j}$ and $B_{3j}$ (2.21*a*, *b*) or (B1), (B2) has no solution if the segment of the generating arc for any surface element is perpendicular to the axis. This difficulty arises because the coefficient of the first term in (B2) vanishes if $\theta_j = \frac{1}{2}\pi$. In the prolate spheroid representation described in § 4 this problem could easily be circumvented by a numerical approximation scheme, since the portions of surface with vertical tangents were confined to just the two end points of the spheroid. For objects with flat end surfaces, such as the ends of a circular cylinder or the base of a cone, the problem of accurate end representations is obviously more critical.

The general technique for handling axially perpendicular surface elements is closely related to the multipole truncation procedure developed for spheres and spheroids in Gluckman *et al.* (1971). Inspection of (2.3) and (2.5) shows that for $\theta_j = \frac{1}{2}\pi$, $q_j = 0$ and all the odd-order terms in (2.3) vanish since $I_n(0) = 0$ for $n$ odd. The infinite series of even-order terms in (2.3) in the limit $b = 0$ provides a complete set of functions to satisfy the no-slip boundary conditions on the surface of a disk for any distribution of singularities in the rest of the flow field. For example, if the sole singularity is a uniform source at infinity, only the $n = 2$ terms are required, as shown in the discussion of (2.23), to satisfy the viscous-flow boundary conditions on the disk surface. For an arbitrary body of revolution with a blunt base or forward face, singularities of the form (3.1) will be distributed over the entire remaining surface of the object. These singularities will in general produce a complicated disturbance over the perpendicular surfaces, and require the use of all even-order singularities in (2.3) with $b = 0$ to satisfy the no-slip boundary conditions exactly at all points. However, in the spirit of Gluckman *et al.* approximate end representations, which approach the exact solution to any desired order of accuracy, can be achieved by truncating the series and satisfying the no-slip boundary conditions at discrete points along the generating line for each axially perpendicular surface. Each set of $B_{nj}$ and $D_{nj}$ coefficients in this series provide the freedom to satisfy the real-fluid boundary conditions at one discrete point on this generating line. Thus, the total solution for the stream function for an arbitrary convex body of revolution consists of the summation of a free-stream contribution $\psi_\infty$, the superposition integral in (3.2) and an infinite series obtained from (2.3) with $n$ even and $b = 0$ placed at the axial location of each axially perpendicular portion of surface. Finally, in the numerical solution the linear matrix of equations (B1), (B2) must be enlarged to include the truncated series representing each perpendicular surface and the values of all the unknown coefficients determined by a simultaneous solution of this enlarged matrix equation.

To take advantage of the computer program developed in Gluckman *et al.*

(1971) the solution procedure described above for treating perpendicular surface elements had to be modified to take account of the fact the program in Gluckman *et al.* did not allow for spheroidal singularities with zero aspect ratios. In the numerical results presented in §§ 5.1 and 5.2 small but finite aspect ratio spheroidal singularities were used to describe blunt end effects. The boundary points at which the no-slip boundary conditions were satisfied were therefore chosen to lie on the $p = p_0$ co-ordinate surface corresponding to the aspect ratio of the end singularities rather than the actual cone or cylinder surface. To this end, the solutions obtained describe cones and cylinders with varying degrees of bluntness.

### 5.1. *Results for finite cylinders*

The techniques described in § 5.1 and in §§ 3 and 4 will now be applied to determine the drag on short finite cylinders. The convergence characteristics of this new solution procedure will be indicated and the solutions compared with existing experimental data when available.

It has been pointed out by Happel & Brenner (1965) that no previous theoretical treatment is available for creeping motion relative to cylinders with aspect ratios of less than approximately five. However, a large amount of experimental data exists in this area. Before comparing the results for flow past short cylinders computed as described above with experimental results, the method used for describing settling rates will be outlined.

The settling factor $K$ is defined as the ratio of the terminal settling velocity of the body under consideration to the settling velocity of a perfect sphere having the same volume as the object. The Stokes law drag force acting on the sphere having the same volume as the cylinder is

$$F_s = 6\pi\mu U_s r_s, \tag{5.1}$$

where $U_s$ is the settling velocity of the sphere and $r_s$ is its radius. The drag force on a cylinder of radius $r_n$ can be written in the same form as (5.1) by introducing a multiplication factor $\lambda$ which depends only on the geometry of the cylinder. Thus,

$$F_c = 6\pi\mu U_c r_n \lambda, \tag{5.2}$$

where $U_c$ is the settling velocity of the cylinder. From (5.1) and (5.2), $F_c = F_s$ if

$$U_c/U_s = (r_s/r_n)/\lambda, \tag{5.3}$$

where if the sphere and cylinder are to have equal volumes, $r_s = (\frac{3}{4}r_n^2 h)^{\frac{1}{3}}$, $h$ being the cylinder length. Thus, the settling factor $K$ is defined as

$$K = U_c/U_s = (r_s/r_n)/\lambda. \tag{5.4}$$

In accord with our previous remarks the cylinder will be represented by oblate spheroidal singularities distributed at $N$ origins along the cylinder axis. The $N-2$ interior sets of singularities are equally spaced and involve only the two lowest-order spheroidal multipoles, whereas the end singularities will in the general case have a much finer aspect ratio, the number of end multipoles retained depending on the number of discrete boundary points at which the no-slip boundary conditions are to be satisfied on the $p = p_0$ co-ordinate surface

| $\frac{\text{Length}}{\text{Diameter}} = \frac{h}{2r_n}$ | No. of points, $N$ | Aspect ratio, $a/b$ | $K$, this work | $K$, Heiss & Coull | $K$, eqn. (5.5) |
|---|---|---|---|---|---|
| 0·25 | 2 | 0·125 | 0·776 | 0·762 | 0·759 |
| | 3 | 0·083 | 0·759 | | |
| | 5 | 0·050 | 0·746 | | |
| | 7 | 0·036 | 0·742 | | |
| | 9 | 0·028 | 0·738 | | |
| 0·50 | 2 | 0·250 | 0·918 | 0·864 | 0·881 |
| | 3 | 0·167 | 0·892 | | |
| | 5 | 0·100 | 0·869 | | |
| | 7 | 0·071 | 0·857 | | |
| | 9 | 0·056 | 0·856 | | |
| 1·00 | 3 | 0·333 | 1·038 | 0·958 | 0·976 |
| | 5 | 0·200 | 1·000 | | |
| | 7 | 0·143 | 0·974 | | |
| | 9 | 0·111 | 0·950 | | |
| | 11 | 0·091 | 0·945 | | |
| 2·00 | 3 | 0·667 | 1·057 | 0·975 | 1·009 |
| | 5 | 0·400 | 1·020 | | |
| | 7 | 0·286 | 1·004 | | |
| | 9 | 0·222 | 0·994 | | |
| | 11 | 0·182 | 0·986 | | |
| | 13 | 0·154 | 0·983 | | |
| 3·0 | 5 | 0·600 | 1·010 | 0·958 | 0·989 |
| | 7 | 0·429 | 0·996 | | |
| | 9 | 0·333 | 0·986 | | |
| | 11 | 0·273 | 0·979 | | |
| | 13 | 0·231 | 0·974 | | |
| | 15 | 0·200 | 0·970 | | |
| 4·0 | 5 | 0·800 | 0·989 | 0·929 | 0·961 |
| | 7 | 0·571 | 0·973 | | |
| | 9 | 0·444 | 0·964 | | |
| | 11 | 0·364 | 0·956 | | |
| | 13 | 0·308 | 0·951 | | |
| | 15 | 0·267 | 0·947 | | |

TABLE 1. Comparison of settling factors for short cylinders with experimental results of Heiss & Coull (1952) and empirical results of Happel & Brenner (equation (5.5)), without special consideration for end effects.

for the end singularities. The spacing for the discrete point distribution is determined by the condition that the $p = p_0$ co-ordinate surfaces for each adjacent set of singularities be touching. Thus,

$$h = 2(N-2)\,a + 4a_e, \quad r_n = b,$$

$a_e$ is the minor radius of $p = p_0$ co-ordinate surfaces for end spheroidal singularities, $a$ is the minor radius of $p = p_0$ co-ordinate surfaces for interior spheroidal singularities, $b$ is the major radius of $p = p_0$ co-ordinate surfaces for all spheroidal singularities.

Finally, Happel & Brenner (1965) present an empirical correlation for

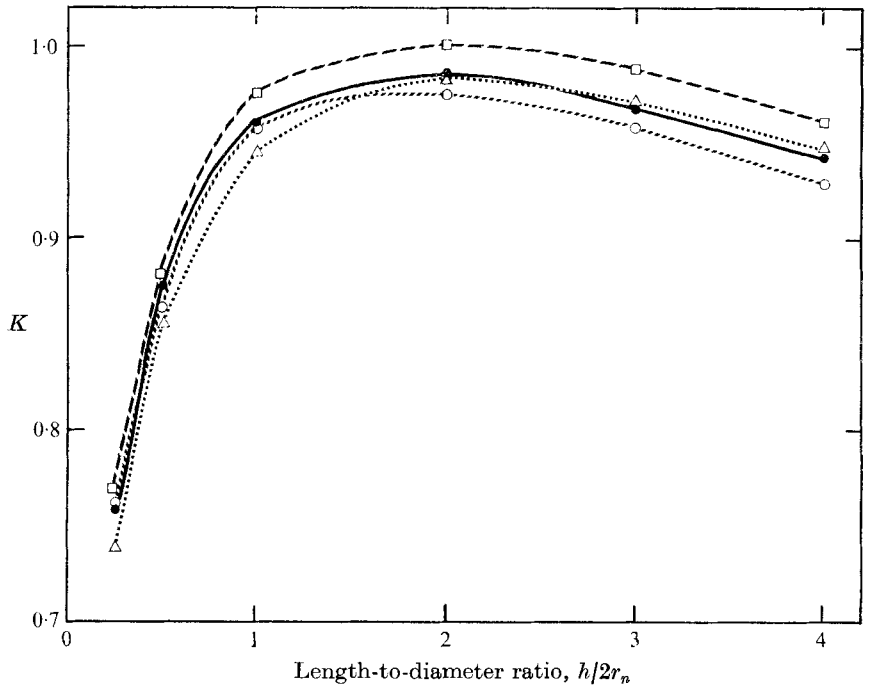


FIGURE 4. Settling factors for short circular cylinders: ○, experimental data of Heiss & Coull; □, empirical data of Happel & Brenner; △, this study, table 1; ●, this study, table 4.

calculating the settling rates based on experimental results obtained for a number of axisymmetric bodies, i.e.

$$\log_{10} K = \log_{10}\left(\frac{r_s}{r_n}\Psi^{\frac{1}{2}}\right) - 0{\cdot}25\left(\Psi\frac{r_s}{r_n}\right)^{\frac{1}{2}}\left(\frac{r_s}{r_n} - 1\right), \tag{5.5}$$

where the sphericity $\Psi$ is defined as the ratio of the area of a sphere of the same volume as the particle to the area of the particle itself.

To illustrate the importance of end effects, several sets of numerical experiments were conducted, and the results were compared with both the experimental data of Heiss & Coull (1952) and the empirical predictions of (5.5). In the first set of experiments shown in table 1, the two lowest-order finite aspect ratio multipoles from which the fundamental solution (2.22) was derived in the limit $b = 0$ were distributed at $N$ equally spaced stations along the cylinder axis. The no-slip boundary conditions on the front and rear surfaces were not satisfied, since the series of higher-order singularities used to describe end effects was omitted.

These results show that-although the settling factor calculated using this first approximation is in reasonable agreement with the experimental and empirical settling results, convergence is not obtained as $N$ is increased. This inability to converge is due to the poor end representations that result when the no-slip boundary conditions are not adequately satisfied near the cylinder ends.

The data in table 1 are plotted in figure 4, where our theoretical values of $K$ are based on the largest value of $N$ for each cylinder. Interestingly, the settling

| No. of $p = p_0$ surfaces, $N$ | End aspect ratio, $a_e/b$ | Central aspect ratio, $a/b$ | No. of multipoles used for end $p = p_0$ surfaces, $M_e$ | $K$ |
|---|---|---|---|---|
| 5 | 0·05 | 0·133 | 2 | 0·852 |
| 5 | 0·05 | 0·133 | 4 | 0·894 |
| 5 | 0·05 | 0·133 | 6 | 0·890 |
| 5 | 0·05 | 0·133 | 8 | 0·890 |
| 5 | 0·05 | 0·133 | 10 | 0·890 |
| 5 | 0·05 | 0·133 | 12 | 0·890 |
| 5 | 0·05 | 0·133 | 14 | 0·890 |
| 5 | 0·15 | 0·067 | 6 | 0·913 |
| 5 | 0·10 | 0·100 | 6 | 0·903 |
| 5 | 0·05 | 0·133 | 6 | 0·890 |
| 5 | 0·03 | 0·147 | 6 | 0·887 |
| 5 | 0·01 | 0·160 | 6 | 0·881 |
| 5 | 0·005 | 0·163 | 6 | 0·880 |
| 3 | 0·05 | 0·400 | 6 | 0·896 |
| 5 | 0·05 | 0·133 | 6 | 0·890 |
| 7 | 0·05 | 0·080 | 6 | 0·890 |
| 9 | 0·05 | 0·057 | 6 | 0·888 |
| 11 | 0·05 | 0·044 | 6 | 0·887 |

TABLE 2. Settling factors for short cylinders ($h/2r_n = 0{\cdot}5$) using higher-order multipoles for ends

rates based on even this first crude use of the multipole truncation technique are in closer agreement with experimental data than the empirical predictions of (5.5). It should be pointed out, however, that the experimental results were not obtained in a fluid of infinite extent. Heiss & Coull (1952) used certain empirical techniques to correct their raw data for wall effects, but no conclusion can be drawn as to how satisfactory these correction methods are.

The second series of numerical experiments reported in table 2 is designed to refine the representation of the ends of the cylinder by using higher-order multipoles to satisfy the no-slip boundary conditions at increasing numbers of points on the generating curves of the end spheroidal singularities. A cylinder having a fixed length-to-diameter ratio of 0·5 was chosen and three sets of calculations performed. The distribution number $N$ of oblate spheroidal singularities ($3 \leqslant N \leqslant 11$) was varied, the aspect ratio $a_e/b$ of the end singularities was varied and finally, the no-slip boundary conditions were satisfied at varying numbers of points $M_e$ ($1 \leqslant M_e \leqslant 13$) on the $p = p_0$ co-ordinate surface of the end spheroidal singularities.

As the first set of results in table 2 show, convergence to three significant figures is obtained when the no-slip boundary conditions are satisfied at only five approximately equally spaced points on the $p = p_0$ co-ordinate surface for the end singularities. One would also conclude from these results that the effect of the higher-order multipoles is localized and does not significantly alter the solution for interior singularities. This rapid convergence of the solution to a desired boundary shape provided the boundary points conform to some natural

co-ordinate system was also exhibited by the multisphere and spheroid solutions presented in Gluckman *et al.* This behaviour suggests that improved end representations should be obtained not by satisfying boundary conditions at more points along the generating arc of the end $p = p_0$ surfaces, since the solution has converged in this sense, but by choosing end singularities whose aspect ratio corresponds more closely to the geometry of the cylinder ends. The second set of calculations shown in table 2 shows the effect of decreasing the aspect ratio of the end spheroidal singularities from 0·15 to 0·005. It is evident from these results that end singularities with an aspect ratio of 0·01 or less yield drag results that have converged to roughly 0·1 % and should therefore accurately represent the cylinder ends.

The third set of results in table 2 shows the effect of increasing the number of interior boundary points for a fixed end representation. The results indicate that the convergence of the solution in the interior region as $N$ increases is satisfactory, and provides drag results accurate to roughly 0·5 % for aspect ratios of 0·2 or less on central spheroids.

The conclusions drawn from tables 1 and 2 concerning the convergence of the solution for the cylinder ends are also supported by the plots of the $\psi = 0$ boundary streamline shown in figures 5 and 6. The touching $p = p_0$ co-ordinate surfaces of the local oblate spheroidal co-ordinate system for each set of singularities are included for reference in both figures. Figure 5 corresponds to the first set of experiments described in table 1, in which only the two lowest-order multipoles are used for each discrete point element including the cylinder ends. The failure of this solution to satisfy the no-slip boundary conditions on the front and rear faces of the cylinders is evident from the large deviation of the theoretically predicted $\psi = 0$ curve from the actual cylinder boundary shown dashed in the figure. Figure 6 shows the results obtained for the $\psi = 0$ boundary when a truncated series of low aspect ratio multipoles are used to describe end effects. For the case shown the no-slip boundary conditions were satisfied at 13 points on the $p = p_0$ co-ordinate surface of an end spheroid whose aspect ratio was 0·05. The greatly improved representation of the $\psi = 0$ boundary at the cylinder ends is self-evident. The second $\psi = 0$ streamline in this figure represents an interior circulation with very low velocity entrained eddies that has no physical significance for the exterior flow. The magnitude of the velocity in the entrained eddies is a measure of the magnitude by which the no-slip boundary conditions are violated on the approximate $\psi = 0$ boundary streamline between boundary points. Maximum velocities on this streamline were less than one-thousandth of the free-stream velocity for the computation shown in figure 6.

Finally, table 3 presents data for flow past short cylinders of various length-to-diameter ratios and compares settling factors with those of Heiss & Coull (1952). It can be seen that, as the number of singularities used to represent each cylinder is increased, the settling factor appears to asymptote to a value that is in excellent agreement with the experimentally measured values of $K$. Some of the improved results from table 3 which include the cylinder end corrections have been plotted in figure 4. These results are in better agreement with the experimental data at the low length-to-diameter ratios than are the previous

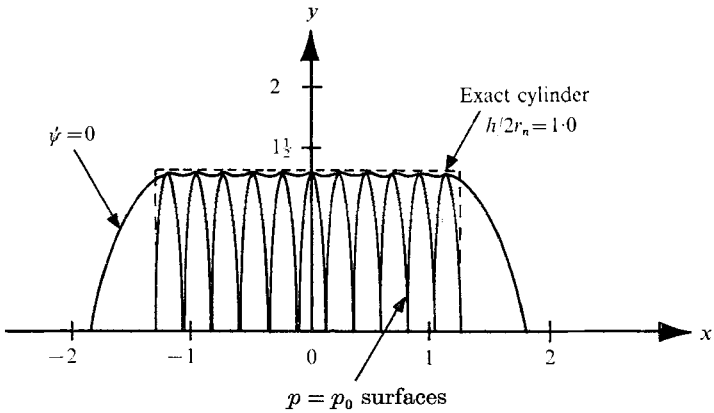


FIGURE 5. $\psi = 0$ boundary streamline for short cylinder with aspect ratio = 1·0 neglecting end singularities.

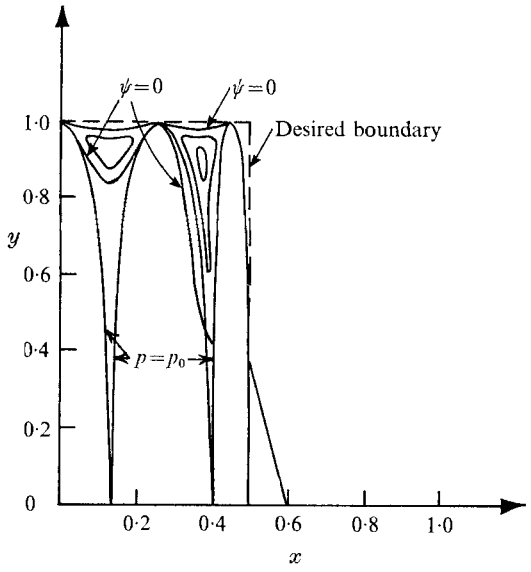


FIGURE 6. $\psi = 0$ boundary streamline for short cylinder with aspect ratio = 0·5 using a truncated series of end singularities. $a = 0{\cdot}133$, $a_e = 0{\cdot}05$, $N = 5$, $M_e = 13$.

settling factors presented in table 1. This improvement is in accord with the fact that the end corrections become increasingly important as the length-to-diameter ratio of the cylinder decreases.

### 5.2. *Results for blunt end cone*

As an example of a non-analytic boundary shape whose generating curve is a function of axial distance we next consider the creeping flow past a right circular cone of apex angle $\theta$. The solution technique employed is similar to that used to represent short cylinders. The end (or base) of the cone is represented by oblate spheroidal singularities of low aspect ratio $a_e/b_e$ using higher-order multipoles to satisfy more accurately the no-slip boundary conditions on the terminal

| $\frac{\text{Length}}{\text{Diameter}} = \frac{h}{2r_n}$ | No. of inscribed $p = p_0$ surfaces, $N$ | End aspect ratio, $a_e/b$ | Central aspect ratio, $a/b$ | No. of multipoles used for end representation, $M_e$ | $K$, this work | $K$, Heiss & Coull (1952) |
|---|---|---|---|---|---|---|
| 0·25 | 3 | 0·05 | 0·150 | 5 | 0·775 | 0·762 |
| | 7 | 0·05 | 0·030 | 5 | 0·773 | |
| | 11 | 0·05 | 0·017 | 5 | 0·772 | |
| | 3 | 0·005 | 0·240 | 5 | 0·764 | |
| | 7 | 0·005 | 0·048 | 5 | 0·760 | |
| | 11 | 0·005 | 0·027 | 5 | 0·759 | |
| 0·5 | 3 | 0·05 | 0·400 | 5 | 0·896 | 0·864 |
| | 7 | 0·05 | 0·080 | 5 | 0·890 | |
| | 11 | 0·05 | 0·044 | 5 | 0·887 | |
| | 3 | 0·005 | 0·490 | 5 | 0·884 | |
| | 7 | 0·005 | 0·098 | 5 | 0·878 | |
| | 11 | 0·005 | 0·054 | 5 | 0·877 | |
| 1·0 | 5 | 0·05 | 0·300 | 5 | 0·975 | 0·958 |
| | 9 | 0·05 | 0·129 | 5 | 0·971 | |
| | 11 | 0·05 | 0·100 | 5 | 0·969 | |
| | 5 | 0·005 | 0·330 | 5 | 0·967 | |
| | 9 | 0·005 | 0·141 | 5 | 0·961 | |
| | 11 | 0·005 | 0·110 | 5 | 0·960 | |
| 2·0 | 5 | 0·05 | 0·633 | 5 | 1·002 | 0·975 |
| | 9 | 0·05 | 0·271 | 5 | 0·994 | |
| | 11 | 0·05 | 0·211 | 5 | 0·993 | |
| | 5 | 0·005 | 0·663 | 5 | 0·997 | |
| | 9 | 0·005 | 0·284 | 5 | 0·988 | |
| | 11 | 0·005 | 0·221 | 5 | 0·986 | |
| 3·0 | 7 | 0·05 | 0·580 | 5 | 0·979 | 0·958 |
| | 9 | 0·05 | 0·414 | 5 | 0·976 | |
| | 11 | 0·05 | 0·322 | 5 | 0·961 | |
| | 7 | 0·005 | 0·598 | 5 | 0·974 | |
| | 9 | 0·005 | 0·427 | 5 | 0·971 | |
| | 11 | 0·005 | 0·332 | 5 | 0·969 | |
| 4·0 | 7 | 0·05 | 0·780 | 5 | 0·952 | 0·929 |
| | 9 | 0·05 | 0·557 | 5 | 0·949 | |
| | 11 | 0·05 | 0·433 | 5 | 0·947 | |
| | 7 | 0·005 | 0·798 | 5 | 0·948 | |
| | 9 | 0·005 | 0·570 | 5 | 0·945 | |
| | 11 | 0·005 | 0·443 | 5 | 0·943 | |

TABLE 3. Settling factors for short cylinders ($0{\cdot}25 \leqslant h/2r_n \leqslant 4{\cdot}0$) using higher order multipoles for the ends

$p = p_0$ co-ordinate surface. This permits the higher-order multipoles to produce an accurate representation of the base of the cone that will converge to the true planar shape as the aspect ratio of the end spheroidal singularities approaches zero. The rest of the cone interior is divided into $N$ sections of equal axial distance.

The section closest to the apex can be treated to any order of accuracy by subdividing this first section into any number of smaller sections. Except for

| No. of inscribed $p = p_0$ surfaces, $N$ | Minor axis of end spheroid, $a_e$ | Minor axes of other spheroids, $a$ | No. of multipoles used for end representation, $M_e$ | $\lambda$ |
|---|---|---|---|---|
| 15 | 0·05 | 0·0544 | 2 | 0·8774 |
| 15 | 0·05 | 0·0544 | 4 | 0·8666 |
| 15 | 0·05 | 0·0544 | 6 | 0·8710 |
| 15 | 0·05 | 0·0544 | 8 | 0·8712 |
| 15 | 0·05 | 0·0544 | 10 | 0·8713 |
| 15 | 0·05 | 0·0544 | 12 | 0·8713 |
| 9 | 0·005 | 0·0957 | 8 | 0·8925 |
| 9 | 0·01 | 0·0951 | 8 | 0·8899 |
| 9 | 0·03 | 0·0929 | 8 | 0·8801 |
| 9 | 0·10 | 0·0851 | 8 | 0·8466 |
| 9 | 0·15 | 0·0796 | 8 | 0·8234 |
| 9 | 0·20 | 0·0740 | 8 | 0·8010 |
| 3 | 0·005 | 0·2870 | 8 | 0·8877 |
| 5 | 0·005 | 0·1722 | 8 | 0·8908 |
| 7 | 0·005 | 0·1230 | 8 | 0·8923 |
| 9 | 0·005 | 0·0957 | 8 | 0·8925 |
| 11 | 0·005 | 0·0783 | 8 | 0·8926 |
| 13 | 0·005 | 0·0662 | 8 | 0·8928 |
| 15 | 0·005 | 0·0574 | 8 | 0·8931 |

TABLE 4. Drag correction factor $\lambda$ (5.8) for a 60° cone $r_n = 1$

the base representation, only the two lowest-order multipoles are to be used. Convergence to the exact conical boundaries can be expected as the number of boundary points approaches infinity using the same arguments presented in the discussion of the cylinder.

Drag results will be presented for flow past a 30° half-angle cone represented by a discrete distribution of $N$ sets of spheroidal singularities ($3 \leqslant N \leqslant 15$) when the no-slip boundary conditions are satisfied at $M_e$ points ($2 \leqslant M_e \leqslant 14$) on the generating arc of the $p = p_0$ co-ordinate surface closest to the base of the cone. These results will be reported in a terminology consistent with that used for the case of flow past cylinders.

From (3.7) the total drag force on the cone is

$$F_0 = 4\pi\mu \sum_{j=1}^{N} \frac{D_{2j}}{C_j}. \tag{5.6}$$

$F_0$ can be related to the Stokes drag on a sphere having the same diameter as the cone (at its base) by introducing a multiplicative factor $\lambda$:

$$F_0 = 6\pi\mu U r_n \lambda, \tag{5.7}$$

where $r_n$ is the radius of the base of the cone. Equating (5.6) and (5.7) one obtains

$$\lambda = \frac{1}{1{\cdot}5 U r_n} \sum_{j=1}^{N} \frac{D_{2j}}{C_j}. \tag{5.8}$$

Some of the results for flow past a 30° half-angle cone are presented in table 4. Three sets of numerical experiments were performed to show the dependence of the accuracy of the solution on (i) the number of elements $N$ in the distribution, (ii) the aspect ratio of the end singularities, and (iii) the number of multipoles used to satisfy the no-slip boundary conditions on the $p = p_0$ surface for the base of the cone. The trends of the results shown in table 4 are similar to those discussed in table 2 for the cylinder. With other factors held constant, $\lambda$ converges to four significant digits when 8 multipoles are used to satisfy the boundary conditions at equally spaced points along the generating arc of the end $p = p_0$ co-ordinate surface. $\lambda$ is a sensitive function of the aspect ratio of the end singularity. If the results of the second set of calculations are linearly extrapolated to $a_e = 0$ one obtains a value for $\lambda$ of 0·895. Finally, increasing $N$ beyond 7 produces changes in $\lambda$ that are of the order 0·1 % or less.

## 6. Approximations for long finite cylinders

In theory, the elemental oblate spheroidal singularity construction technique described in §§2–5 can be applied to the creeping flow past an arbitrary convex body of revolution. A practical limitation exists, however, for bodies of high aspect ratio. If one wishes to minimize the error in the drag computed from (3.8), a large number of singularities of low aspect ratio would be required for the representation. For example, to represent a cylinder having a length-to-diameter ratio of 40 using elemental oblate spheroidal singularities of aspect ratio 0·05 would require 800 multipoles excluding end effects. To determine the four unknown coefficients in the two lowest-order multipoles describing each surface element would involve the solution of 3200 linear simultaneous algebraic equations.

A simple yet good engineering approximation to the flow past high aspect ratio bodies will now be developed and applied to long finite cylinders. We shall show that the drag on such elongated objects can be well approximated by a series of prolate spheroidal singularities with touching $p = p_0$ co-ordinate surfaces. The details of the solution for the stream function for flow past multiple prolate spheroids is given in Gluckman *et al.* (1971). The basic solution is equation (2.3), now modified so that $p_j$ and $q_j$ apply to prolate spheroidal co-ordinates:

$$p_j = \cosh \xi_j = \frac{R_{1j} + R_{2j}}{2c}, \quad q_j = \cos \eta_j = \frac{R_{2j} - R_{1j}}{2c},$$

$$R_{1j} = [(x - 2jd - c)^2 + y^2]^{\frac{1}{2}}, \quad R_{2j} = [(x - 2jd + c)^2 + y^2]^{\frac{1}{2}}.$$

Convergence of this representation technique for long cylinders cannot be expected, since the no-slip boundary conditions will not be satisfied exactly on either the lateral surface of the cylinder or its ends. The errors due to end effects, however, should be relatively unimportant for very extended objects. Drag correction factors for long cylinders based on prolate spheroidal representation are compared with Burger's approximate solution,

$$F_c = \frac{2\pi\mu U_c h}{\ln (h/r_n) - 0{\cdot}72}, \tag{6.1}$$

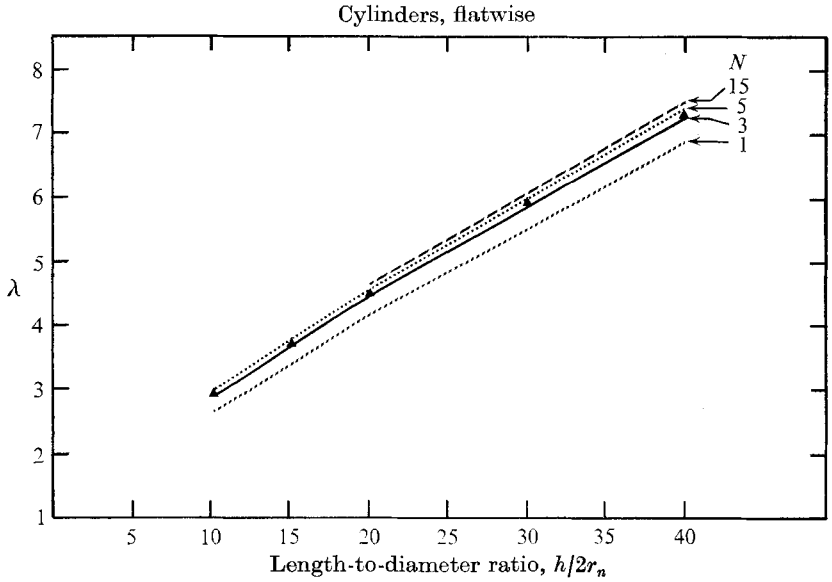


FIGURE 7. Comparison of present approximate solutions for high aspect ratio prolate spheroid with Burgers's approximate results: $N$ = number of prolate spheroids; ▲, Burgers's predicted values.

| $\frac{\text{Length}}{\text{Diameter}} = \frac{h}{2r_n}$ | No. of spheroidal elements, $N$ | Aspect ratio, $a/b$ | $\lambda$ this work | $\lambda$ eqn. (6.3) |
|---|---|---|---|---|
| 10·0 | 1 | 10·0 | 2·647 | 2·929 |
| | 2 | 5·0 | 2·815 | |
| | 3 | 3·3333 | 2·883 | |
| | 5 | 2·0 | 2·946 | |
| 20·0 | 1 | 20·0 | 4·172 | 4·490 |
| | 2 | 10·0 | 4·384 | |
| | 3 | 6·6667 | 4·469 | |
| | 5 | 4·0 | 4·548 | |
| | 9 | 2·2222 | 4·611 | |
| | 15 | 1·3333 | 4·651 | |
| 40·0 | 1 | 40·0 | 6·859 | 7·280 |
| | 2 | 20·0 | 7·150 | |
| | 3 | 13·3333 | 7·265 | |
| | 5 | 8·0 | 7·370 | |
| | 9 | 4·4444 | 7·450 | |
| | 15 | 2·6667 | 7·496 | |

TABLE 5. Comparison of drag correction factors for long cylinders calculated from the multipole technique, with approximation of Burgers

based on the point force technique in table 5. From the definition of $\lambda$ the force on the cylinder can be represented by

$$F_c = 6\pi\mu U_c r_n \lambda. \tag{6.2}$$

Equating (6.1) and (6.2)
$$\lambda = \frac{h}{\{3r_n[\ln(h/r_n) - 0{\cdot}72]\}}. \tag{6.3}$$

Table 5 demonstrates that good approximations to the drag on long cylinders can be achieved by this technique. For the reasons mentioned above, convergence is not achieved using any reasonable number of prolate spheroidal singularities. The results of table 5 are presented graphically in figure 7. It can be seen that the closest approximation to Burgers' results always seem to occur when the cylinder is represented by between three and five prolate spheroidal elements.

M.J.G. wishes to acknowledge the support and encouragement provided by the St Regis Paper Company. The numerical computations described in this study were performed in partial fulfilment of the requirements for the Ph.D. degree from the School of Engineering of The City College of The City University of New York and are contained in the Ph.D. thesis of M.J.G. (1971). S.W. and R.P. thank the National Science Foundation for supporting this research under grant GK-16506.

## Appendix A

Sampson (1891) has shown that the solution for the stream function to the creeping motion axisymmetric flow equation can be represented by an infinite series of simple separable solutions placed at the origin of a given orthogonal co-ordinate system. In spherical co-ordinates for flow in an unbounded medium the series can be represented by

$$\psi = \tfrac{1}{2}A_2 r^2 \sin^2\theta + \sum_{n=2}^{\infty} [B_n r^{-n+1} + D_n r^{-n+3}]\, I_n(\cos\theta). \tag{A1}$$

The series of Gegenbauer functions represents a series of multilobular disturbances emanating from the origin. The constants inside the brackets determine the strength of each multipole in the series and provide the freedom to satisfy the no-slip boundary conditions at one point on the generating arc of the submerged object. Sampson has also shown that for flow past a perfect sphere only the first multipole ($n = 2$) is required to represent exactly the no-slip boundary conditions, i.e. the strengths of all the higher-order multipoles are identically zero. O'Brien (1968) and Hyman (1970) have shown that good numerical approximations can be obtained for slightly deformed spheres by including the effects of higher-order multipoles from the solution set represented by (A1).

Before the limitations of this approach were fully understood, the authors attempted to extend the results of O'Brien by applying the same procedure to represent objects of greater eccentricity than those considered by earlier workers. In particular, prolate spheroids of different aspect ratios were chosen as the bodies to be represented by the spherical multipole series, as exact solutions for these objects were readily available in the literature.

Two numerical experiments were conducted. First, solutions for prolate spheroids having aspect ratios from 1·0 to 20·0 were computed, using the first 6 spherical multipoles in the series. The results (table 6) are expressed in terms of the drag correction factor defined in Gluckman *et al.* (1971) and (5.2), and

| Aspect ratio | $\lambda$, this study | $\lambda$, exact |
|---|---|---|
| 1·0 | 1·0 | 1·000 |
| 1·5 | 1·107 | 1·102 |
| 2·0 | 1·820 | 1·204 |
| 3·0 | 2·461 | 1·405 |
| 5·0 | 3·987 | 1·785 |
| 10·0 | 9·359 | 2·647 |
| 20·0 | 18·372 | 4·172 |

TABLE 6. Representation of prolate spheroids of varying aspect ratios, using the first six spherical multipoles in the series

| No. of multipoles retained in the solution | $\lambda$, this study | $\lambda$, exact |
|---|---|---|
| 2 | 1·000 | 1·204 |
| 4 | 1·353 | 1·204 |
| 6 | 1·820 | 1·204 |
| 8 | 3·033 | 1·204 |
| 10 | 2·754 | 1·204 |
| 12 | 2·939 | 1·204 |
| 14 | 3·347 | 1·204 |
| 16 | 1·481 | 1·204 |
| 18 | 4·113 | 1·204 |

TABLE 7. Representation of a prolate spheroid of aspect ratio = 2, using from 2 to 18 spherical multipoles

compared with the exact solutions of Happel & Brenner (1965). It can be seen from these results that, for aspect ratios greater than 1·5, this solution procedure produces estimates of the drag correction factor that diverge rapidly as the aspect ratio increases. The second experiment was an attempt to investigate the convergence characteristics of this procedure by increasing the number of spherical multipoles retained in the solution for a prolate spheroid of prescribed aspect ratio. Thus, a prolate spheroid of aspect ratio 2·0 was described using from 2 to 18 spherical multipoles. The results of this trial are presented in table 7. It is interesting to note from the table that increasing the number of spherical multipoles to represent the grossly distorted sphere (prolate spheroid) results in an unstable oscillatory type of solution, with the amplitude of the oscillations increasing as the number of multipoles is increased.

## Appendix B

In §3 a numerical approximation scheme was devised for the evaluation of (3.5), and its counterpart equation obtained from (3.4) for the vanishing of the $u$ velocity component along the profile curve $y_s(x)$ of the object. In this scheme the no-slip boundary conditions were to be satisfied at the midpoint of the straight line segment used to generate each cone frustrum. For improved

accuracy a different approximation was to be used in the integration over the conical element depending on whether the boundary point at which the no-slip boundary conditions were to be satisfied lay on the element in question or on one of the other conical surface elements. When the boundary point was on the same surface element the kernel of the integral was approximated by the first two terms of the Taylor series obtained from (2.15)–(2.17) and (2.19). When the boundary point was outside the surface element the kernel was treated as a constant in the integration over the surface element. The value of the constant was based on the midpoints of both the element over which the integration was being performed and the element in which the boundary point was located. The results of this integration of (3.3) and (3.4) are given below, where the subscript $j$ denotes the conical element at whose midpoint the no-slip boundary conditions are to be satisfied.

$$\begin{aligned}\frac{\partial \psi_\infty}{\partial x} = &-\frac{1}{6}\left(\frac{l_j}{y_{sj}}\right)^{\frac{3}{2}}\left[i(\pi_{2j}^3-\pi_{1j}^3)\,B_{2j}-(\pi_{1j}\pi_{2j}^2+\pi_{1j}^2\pi_{2j})\,B_{3j}\right]\\ &+\sum_{\substack{i=1\\ i\neq j}}^{N} B_{2i}\left[\frac{\partial p}{\partial x}(Q_1(p)+1)(1-q^2)+2\frac{\partial q}{\partial x}(H_2(p)-p)\,q\right]\Big|_{\substack{x_j=0\\ x_i=0}}\frac{\Delta x_i}{2}\\ &+B_{3i}\left[\frac{\partial p}{\partial x}(Q_2(p)+\tfrac{1}{3})\,(q-q^3)-\frac{\partial q}{\partial x}(H_3(p)-\tfrac{1}{3})\,(1-3q^2)\right]\Big|_{\substack{x_j=0\\ x_i=0}}\frac{\Delta x_i}{2}, \quad \text{(B1)}\end{aligned}$$

$$\begin{aligned}\frac{\partial \psi_\infty}{\partial y} = &-\frac{\cos\theta_j}{6}\left(\frac{l_j}{y_{sj}}\right)^{\frac{3}{2}}\left[i(\pi_{1j}-\pi_{2j})\,B_{2j}-\left(2(\pi_{2j}-\pi_{1j})+\frac{\pi_{1j}^2}{\pi_{2j}}+\frac{\pi_{2j}^2}{\pi_{1j}}\right)B_{3j}\right]\\ &+\sum_{\substack{i=1\\ i\neq j}}^{N} B_{2i}\left[\frac{\partial p}{\partial y}(Q_1(p)+1)\,(1-q^2)+2\frac{\partial q}{\partial y}(H_2(p)-p)\,q\right]\Big|_{\substack{x_j=0\\ x_i=0}}\frac{\Delta x_i}{2}\\ &+B_{3i}\left[\frac{\partial p}{\partial y}(Q_2(p)+\tfrac{1}{3})\,(q-q^3)-\frac{\partial q}{\partial y}(H_3(p)-\tfrac{1}{3})\,(1-3q^2)\right]\Big|_{\substack{x_j=0\\ x_i=0}}\frac{\Delta x_i}{2}, \quad \text{(B2)}\end{aligned}$$

where $j = 1, 2, 3, \ldots, N$ and $\pi_{1j}$ and $\pi_{2j}$ are given in (2.13) with $\theta = \theta_j$.

## REFERENCES


Batchelor, G. K. 1970 *J. Fluid Mech.* **44**, 419.

Burgers, J. M. 1938 *Second Report on Viscosity and Plasticity.* North Holland.

Chen, T. C. & Skalak, R. 1970 *Appl. Sci. Res.* **22**, 403.

Cox, R. G. 1970 *J. Fluid Mech.* **44**, 791.

Cox, R. G. 1971 *J. Fluid Mech.* **45**, 625.

Faxen, H. 1925 *Arkiv. Mat. Astron. Fys.* 19A, no. 13. (Appendix by Dahl.)

Gluckman, M. J., Pfeffer, R. & Weinbaum, S. 1971 *J. Fluid Mech.* **50**, 705.

Gluckman, M. J., Pfeffer, R. & Weinbaum, S. 1972 The unsteady settling of three spheres along their line of centres in a viscous fluid. (To be published.)

Happel, J. & Brenner, H. 1965 *Low Reynolds Number Hydrodynamics.* Prentice-Hall.

Heiss, J. F. & Coull, J. 1952 *Chem. Eng. Prog.* **48**, 133.

Hess, J. L. & Smith, A. M. O. 1966 *Progress in Aeronautical Sciences*, vol. 8. Pergamon.

Hyman, W. A. 1970 Viscous flow of a suspension of deformable liquid drops through a cylindrical tube. Ph.D. thesis, Columbia University.

Kármán, T. von 1930 *N.A.C.A. Tech. Mem.* no. 574.

KELLOG, O. D. 1929 *Foundations of Potential Flow Theory*. Dover.

O'BRIEN, V. 1968 *A.I.Ch.E. J.* **14**, 870.

PAYNE, L. E. & PELL, W. H. 1960 *J. Fluid Mech.* **7**, 529.

PRAEGER, W. 1928 *Phys. Z.* **29**, 865.

SAMPSON, R. A. 1891 *Phil. Trans.* **A182**, 449.

STIMSON, M. & JEFFERY, O. B. 1926 *Proc. Roy. Soc.* **A111**, 110.

STOKES, G. G. 1851 *Trans. Camb. Phil. Soc.* **9** (2), 8.

TAYLOR, G. I. 1969 *Problems of Hydrodynamics and Continuous Mechanics. S.I.A.M. Publications*, p. 718.

TILLETT, J. P. K. 1970 *J. Fluid Mech.* **44**, 401.

TUCK, E. O. 1964 *J. Fluid Mech.* **18**, 619.

TUCK, E. O. 1968 Towards the calculation and minimization of Stokes drag on bodies of arbitrary shape. *3rd Australasian Conf. on Hydraulics and Fluid Mechanics*, Sydney, preprint no. 2584, pp. 25–29.

VANDREY, F. 1964 *Aero. Res. Counc. R. & M.* no. 3374.

WANG, H. & SKALAK, R. 1969 *J. Fluid Mech.* **38**, 75.